A measurable Lawson criterion and hydro-equivalent curves for inertial confinement fusion

C. D. Zhou and R. Betti

Citation: Phys. Plasmas **15**, 102707 (2008); doi: 10.1063/1.2998604
View online: http://dx.doi.org/10.1063/1.2998604
View Table of Contents: http://pop.aip.org/resource/1/PHPAEN/v15/i10
Published by the American Institute of Physics.

A measurable Lawson criterion and hydro-equivalent curves for inertial confinement fusion

C. D. Zhou[1] and R. Betti[1,2]
[1]*Fusion Science Center and Laboratory for Laser Energetics, University of Rochester, Rochester, New York 14623, USA*
[2]*Departments of Mechanical Engineering & Physics and Astronomy, University of Rochester, Rochester, New York 14623, USA*

(Received 16 May 2008; accepted 12 September 2008; published online 30 October 2008; publisher error corrected 4 November 2008)

It is shown that the ignition condition (Lawson criterion) for inertial confinement fusion (ICF) can be cast in a form dependent on the only two parameters of the compressed fuel assembly that can be measured with existing techniques: the hot spot ion temperature (T_i^h) and the total areal density (ρR_{tot}), which includes the cold shell contribution. A marginal ignition curve is derived in the ρR_{tot}, T_i^h plane and current implosion experiments are compared with the ignition curve. On this plane, hydrodynamic equivalent curves show how a given implosion would perform with respect to the ignition condition when scaled up in the laser-driver energy. For $3<\langle T_i^h\rangle_n<6$ keV, an approximate form of the ignition condition (typical of laser-driven ICF) is $\langle T_i^h\rangle_n^{2.6}\cdot\langle\rho R_{\mathrm{tot}}\rangle_n>50$ keV$^{2.6}\cdot$ g/cm^2, where $\langle\rho R_{\mathrm{tot}}\rangle_n$ and $\langle T_i^h\rangle_n$ are the burn-averaged total areal density and hot spot ion temperature, respectively. Both quantities are calculated without accounting for the alpha-particle energy deposition. Such a criterion can be used to determine how surrogate D_2 and subignited DT target implosions perform with respect to the one-dimensional ignition threshold. © *2008 American Institute of Physics*. [DOI: 10.1063/1.2998604]

I. INTRODUCTION

In inertial confinement fusion (ICF),[1,2] a shell of cryogenic deuterium and tritium ice is imploded at high velocities $[(\sim 2-4]\times 10^7$ cm/s) and low entropy to achieve high central temperatures and high areal densities. The final fuel assembly consists of a relatively low density ($\sim$30–80 g/cc) high temperature ($\sim$4–8 keV) core (the hot spot) surrounded by a dense ($\sim$300–1000 g/cc) cold ($\sim$100 eV) fuel layer (the compressed shell). The Lawson criterion[3] determining the onset of thermonuclear ignition is usually expressed through the product $p\tau>10$ atm·s, where p is the plasma pressure in atm and τ is the energy confinement time in seconds. In magnetic fusion devices, both the pressure and confinement time are routinely measured and the performance of each discharge can be assessed by comparing the value of $p\tau$ with respect to the ignition value (10 atm·s). In inertial confinement fusion, both p and τ cannot be directly measured, and the performance of subignited ICF implosions cannot be assessed with respect to the ignition condition. Often, the Lawson criterion is extended to ICF by simply restricting its application to the hot spot and by replacing p with the ideal gas equation of state $p=2\rho_h T_h/m_i$ (ρ_h is the hot spot mass density, T_h is the hot spot temperature, and m_i is the DT average ion mass), and τ with the sound wave traveling time through the hot spot, $\tau\sim R_h/C_s$ (here R_h is the hot spot radius and C_s is the hot spot sound speed, $C_s\sim\sqrt{T_h}$). This leads to the hot spot ignition condition $(\rho_h R_h)\sqrt{T_h}>$const, where $\rho_h R_h$ is the hot spot areal density. There are two problems with such a simple derivation: (a) The confinement time is incorrect since it neglects the inertial confinement of the surrounding cold shell, and (b) the hot spot areal density cannot be experimentally measured.

A more accurate form of the hot spot ignition condition is given in Refs. 1 and 4–6 with the alpha heating balancing all the hot spot power losses (thermal conduction and radiation losses). Our approach to ignition is somewhat different from that in Ref. 4. First, our ignition model is dynamic as it includes both the compression and expansion phases of the shell motion. Second, our ignition condition is given in terms of the total areal density rather than the hot spot areal density. Third, the ignition condition is viewed as an instability of both the pressure and the temperature rather than only the temperature. This causes the heat conduction losses to enter the ignition condition in a fundamentally different way. A more detailed discussion of this point is provided in Sec. II. It is important to emphasize that the presence of a cold dense shell surrounding the hot spot significantly alters the onset of the thermonuclear instability (a similar point is made in Refs. 4, 12, and 18). Since the heat conductivity is negligible in the cold shell, most of the heat leaving the hot spot is recycled back into the hot spot in the form of internal energy and pdV work of the plasma ablated off the inner shell surface. Much of the radiation losses are also recycled back through ablation since the cold shell is opaque to the low-energy portion of the x-ray bremsstrahlung spectrum (only the high-energy x rays can penetrate the dense shell). As is argued in Ref. 12, the heat conduction and, to some extent, the radiation losses do not appreciably change the hot spot pressure (i.e., energy). Instead, those losses raise the density and lower the temperature while keeping $p\sim\rho T$ approximately constant. Since the fusion rate scales as $n^2\langle\sigma v\rangle$, with $\langle\sigma v\rangle\sim T^{3-4}$ for

$T<6-8$ keV and $\langle\sigma v\rangle\sim T^2$ for $6-8<T<25$ keV, it follows that the alpha self-heating is degraded by heat conduction and radiation losses only at low temperatures less than 6–8 keV but unchanged at high temperatures $T>6-8$ keV. This occurs because at high temperatures, the fusion rates depend only on the hot spot pressure ($n^2\langle\sigma v\rangle\sim p^2$) that is independent of the heat losses. While these recycling effects (described in detail in Ref. 12) improve the ignition threshold, the expansion losses, that are often not included in the ignition condition, cause a transfer of internal energy to kinetic energy and degrade the ignition conditions. Since the hot spot expansion occurs against the dense shell, the ignition conditions depend on the inertia of the dense shell. Furthermore, the hot spot internal energy comes from the shell kinetic energy, which is also used to assemble the shell areal density. As shown in Ref. 13, there is a direct correlation between the hot spot areal density and shell areal density. Thus, one can expect that the ICF Lawson criterion depends on the shell areal density.

In this paper, we derive a form of the Lawson criterion that can be directly measured in ICF implosions and includes the confinement of the surrounding cold shell. One can use such a new criterion to assess how far current and future subignited ICF implosions are from achieving ignition. Such a new ignition criterion depends on the only two quantities in the ICF fuel assembly that can be measured with existing techniques: the total areal density and the hot spot ion temperature. Note that the total areal density comes mostly from the cold shell surrounding the hot spot, and is directly related to the inertial confinement time. In cryogenic implosions, the total areal density can be measured through charged particle spectroscopy, or x-ray radiography. The ion temperature is measured with the neutron time of flight (nTOF) diagnostic.[7] For instance, recent cryogenic implosions[8] of D_2 targets on the OMEGA laser[9] have achieved a fusion burn-averaged areal density of 200 mg/cm^2 and burn-averaged ion temperature of 2 keV, the highest performance for a cryogenic implosion to date. The burn-averaged areal density has been measured through the energy downshift of the proton spectrum from the secondary D+He^3 reactions.[10] The ion temperature was measured through the nTOF diagnostic. The ion temperature used in the ignition condition is the temperature computed without the alpha-particle heating. Thus, our measurable Lawson criterion is applicable to D_2 surrogate targets and DT subignited implosions. Ignited DT implosions do not require a theoretical ignition criterion to verify that the ignition conditions have been achieved.

We also show that hydro-equivalent curves can be represented on the same ($\rho R_{\rm tot}$, T_i^h) plane. Hydro-equivalent curves are defined as curves with constant adiabat and implosion velocity. Since the laser energy is the only parameter varying along such curves, they can be used to predict how a given implosion would perform when scaled up to a larger laser. For example, any implosion carried out on the OMEGA laser[9] is represented by a point on a hydro-equivalent curve. By increasing the laser energy and keeping the implosion hydro-equivalent, the point on the diagram moves along the hydro-equivalent curve. If that point ends up within the ignition region for NIF-like energies, then one can conclude that such an OMEGA implosion scales to one-dimensional ignition on the National Ignition Facility[11] (NIF).

The paper is organized as follows. The analytic ignition model is described in Sec. II while its initial conditions are derived in Sec. III. The ignition condition from the analytic model is derived in Sec. IV, and compared with the results of one-dimensional hydrodynamic simulations in Sec. V. The assumptions concerning the alpha-particle confinement are discussed in Sec. VI, and comparison with previous forms of the ignition condition are presented in Sec. VII. The hydro-equivalent curves are derived in Sec. VIII and discussed in the Conclusions (Sec. IX).

II. DYNAMIC MODEL OF THERMONUCLEAR IGNITION

The dynamic model described in this section includes the standard energy losses and sources (heat conduction, radiation losses, alpha heating) as well as the compression and expansion dynamics of a hot spot surrounded by a dense shell. The model describes the assembly phase of the hot spot up to ignition. It does not include the propagation of the burn wave or the disassembly of the ignited fuel. As such, energy gains are not calculated and the focus is restricted to the onset of the thermonuclear instability in the hot spot (i.e., ignition).

In the derivation of the ignition conditions, we closely follow the hydrodynamic model of Refs. 12 and 18. During the assembly of the hot spot, its temperature is high and the flow velocity is less than the hot spot sound speed. Thus, we adopt the subsonic model of Refs. 12 and 18 and neglect the kinetic energy with respect to the internal energy inside the hot spot. We assume that most of the alpha-particles generated from the fusion reactions deposit their energy into the hot spot requiring the hot spot size to exceed the alpha-particle mean free path. This condition depends on the hot spot areal density and temperature and is verified *a posteriori*. The energy losses in the hot spot include heat conduction and bremsstrahlung radiation. The conservation of the hot spot energy, including the pdV work of the shell, the alpha-particle heating, and the conduction and radiation energy losses, can be written in the following simple form:

$$\frac{\partial}{\partial t}\left(\frac{p}{\gamma-1}\right)+\nabla\cdot\left[\vec{u}\left(\frac{\gamma p}{\gamma-1}\right)\right]=\nabla\cdot\kappa(T)\,\nabla T+\frac{\theta\rho^2}{4m_i^2}\langle\sigma v\rangle\varepsilon_\alpha-\nabla\cdot\vec{F},\tag{1}$$

where $\rho(r,t)$, $p(r,t)$, and $\vec{u}(r,t)$ are the hot spot density, pressure, and velocity, respectively. Here γ is the ratio of specific heats or adiabatic index ($\gamma=5/3$) and $\kappa(T)=\kappa_0 T^\nu$ is the Spitzer thermal conductivity with $\nu=5/2$. The second term on the right-hand side of Eq. (1) represents the alpha-particle energy deposition, with θ the absorbed alpha-particle fraction depending on the hot spot areal density and temperature, m_i the ion mass for DT, $\varepsilon_\alpha=3.5$ MeV the alpha-particle energy from DT reactions, and $\langle\sigma v\rangle$ the fusion reaction rate as a function of the ion temperature T. The last term is the bremsstrahlung radiation. The radiation flux $\vec{F}$ is the first

moment of the radiation field over angle[14] integrated over all frequencies. The radiation flux $\vec{F}$ depends on both the bremsstrahlung emission and absorption processes. The bremsstrahlung emission[1,15] from the hot spot plasma is expressed in terms of its pressure and temperature as $j=C_1p^2T^{-3/2}$, where $C_1\approx 3.88\times 10^{-29}Z^3/(1+Z)^2$ in $\mathrm{m\cdot J^{5/2}\cdot s^{-1}\cdot N^{-2}}$, pressure p in $\mathrm{N/m^2}$, temperature T in J, and j in $\mathrm{W/m^3}$.

Inside the hot spot, the temperature is high and the plasma is optically thin. At the interface of the hot spot and the cold shell, the temperature drops significantly and much of the radiation energy escaping the hot spot is absorbed near the inner shell surface. The mean free path (l) of photons[1,15] with energy $h\nu$ in a DT plasma is

$$l \approx 2.25\times 10^4 \frac{\sqrt{T}(h\nu)^3}{\rho^2}, \tag{2}$$

where l is in μm, ρ is the plasma density in $\mathrm{g/cm^3}$, T is the plasma temperature in keV, and $h\nu$ is in keV. Consider the free-free emission in a marginally ignited hot spot of typical radius $\sim 50\ \mu$m, temperature 5 keV, and density $\sim 50\ \mathrm{g/cm^3}$. Most of the radiation energy is carried by photons with energy below 5 keV. According to Eq. (2), the mean free path of 5 keV photons ($l\sim 2500\ \mu$m) is much larger than the hot spot size. Therefore, typical hot spots are transparent to bremsstrahlung radiation. On the contrary, a 5 keV photon has a very short mean free path in the cold shell surrounding the hot spot. For typical compressed shell densities of $\sim 600\ \mathrm{g/cm^3}$ and temperatures of ~ 200 eV, the mean free path of a 5 keV photon is only 3.5 μm, much shorter than the typical dense shell thickness 50 μm. This shows that in the fuel assembly of typical ICF implosions, the hot spot is optically thin and the opacity increases sharply near the shell inner surface, resulting in a narrow absorption zone with strong attenuation at the hot spot–shell interface.

For typical ICF plasmas near stagnation, the hot spot temperature is large enough that its sound speed exceeds the flow velocity. The fuel assembly develops an isobaric configuration[12,17,18] and the hot spot has a flat pressure profile with $p\approx p(t)$. The temperature of the high-density shell is much less than that of the low-density hot spot. By neglecting the radiation energy, a self-similar solution for the hot spot temperature[12] is obtained as $T=T_0\hat{T}(\hat{r})$, where T_0 is the central temperature in the hot spot, and $\hat{r}$ is the radius r normalized to the hot spot radius R_h as $\hat{r}=r/R_h$, $\hat{T}\approx(1-\hat{r}^2)^{2/5}/(1-0.15\hat{r}^2)$. This profile indicates $T(\hat{r}=1)\to 0$ at the boundary between the hot spot and the shell. The radiation flux reaching the hot spot boundary is $F(R_h)=\int_0^{R_h} jr^2dr = C_1p^2T_0^{-3/2}R_h^3\int_0^1\hat{T}^{-3/2}\hat{r}^2d\hat{r}$. This radiation flux is absorbed and recycled back into the hot spot with the ablated material at the inner shell surface. As the heat conduction losses are also recycled back into the hot spot via the ablated shell material, both effects alter the hot spot temperature evolution without appreciably changing the pressure.

After integrating Eq. (1) from 0 to the hot spot radius $R_h(t)$, the heat conduction and radiation terms vanish since, as stated above, most of the heat and radiation fluxes are absorbed near the inner shell surface. Thus, the volume integral of the energy equation (1) yields

$$\frac{1}{2}\dot{p}R_h^3+\frac{5}{2}pR_h^2u(R_h,t)=\frac{p^2R_h^3}{(1+Z)^2}\int_1^0\hat{r}^2\frac{\theta\varepsilon_\alpha\langle\sigma v\rangle}{4T^2}d\hat{r}, \tag{3}$$

where $\dot{p}$ is the time derivative of the pressure and $u(R_h,t)$ is the flow velocity at the shell's inner surface. The shell material is ablated into the hot spot as a result of the heat and radiation energy deposited at the inner shell surface. The flow velocity resulting from the combination of the inner surface motion and the ablative flow is

$$u(R_h,t)=\dot{R}_h-V_a, \tag{4}$$

where V_a is the ablation velocity and $\dot{R}_h$ scales with the implosion velocity. Since $V_a\ll\dot{R}_h$, the ablation velocity can be neglected and Eq. (3) can be rewritten in the following form:

$$\frac{d}{dt}(pR_h^3)+2pR_h^2\dot{R}_h=\frac{2p^2R_h^3}{(1+Z)^2}f(T). \tag{5}$$

Notice that pR_h^3 is proportional to the total internal energy of the hot spot and $pR_h^2\dot{R}_h$ to the pdV work. The function $f(T)$, defined as $f(T)\equiv\theta\varepsilon_\alpha/4\int_0^1\hat{r}^2\langle\sigma v\rangle/T^2d\hat{r}$, represents the alpha-particle heating with the fusion reactivity being a function of the temperature T. Observe that $f(T)$ is constant if $\langle\sigma v\rangle$ is approximated with a quadratic power-law dependence on the temperature.

Some of the points made here about the recycling of the heat conduction losses into the hot spot were also highlighted in Refs. 12, 17, and 18. In Ref. 17, it was also argued that a similar effect applies to the alpha particles leaving the hot spot. That is, the alpha particles leaving the hot spot are efficiently stopped by the dense shell within a narrow layer, thus causing ablation of the dense shell material into the hot spot. The ablated material would recycle the alpha-particle energy back into the hot spot in the form of internal energy of the ablated material. As argued in Ref. 17, like heat conduction, alpha-particle losses do not lead to a lower hot spot energy (i.e., pressure) but only to a lower temperature. In this optimistic scenario, the parameter θ in Eq. (1) would be close to unity since all the alpha-particle energy is retained within the hot spot. In our model, we set $\theta\approx 1$ and verify *a posteriori* whether the hot spot areal density is large enough to confine most of the alphas (see Sec. VI).

In order to simplify the analysis, we use a simple numerical fit of $f(T)$ as a power law of the temperature $f(T)=(\varepsilon_\alpha T_*^\sigma/4c_k^{2+\sigma})C_0\hat{T}^\sigma$ after integration over the hot spot volume, where $c_k=1.6\times 10^{-16}$ J/keV, $\varepsilon_\alpha=5.6\times 10^{-13}$ J, $C_0\approx 2.6\times 10^{-26}\ \mathrm{m^3\cdot keV^{-3}\cdot s^{-1}}$ for $\sigma=1$, and T_* in J is defined later in Eq. (8). A comparison between the numerical fit and the accurate values of the fusion reaction rate from Ref. 16 is shown in Fig. 1 for temperature in the range of 3–8 keV. It is important to notice that the fusion reactivity follows a T^3 power law for temperatures $3<T<8$ keV and a T^2 power law for $8<T<25$ keV. In order to accurately capture the onset of the thermonuclear instability, we use a T^3 fit that is more accurate near the ignition threshold temperatures below 8 keV. Using a power-law dependence of the fusion reactiv-

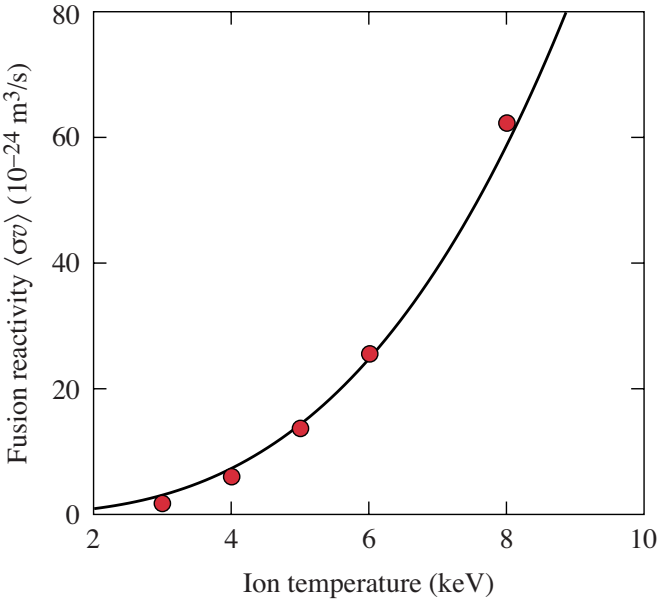

FIG. 1. (Color online) Fusion reactivity $\langle \sigma v \rangle$ is plotted as a power law $\propto T^3$ (solid line). The dots are the reactivity data taken from Ref. 16.

ity also helps to define the onset of the ignition process. In the power-law model, the thermonuclear instability does not saturate since the fusion burn continues until the fuel is depleted. This causes the solution of the ignition model to develop an explosive instability or mathematical singularity. It follows that one can identify the onset of ignition with the development of the mathematical singularity. This can be easily explained by observing that in the absence of plasma motion ($\dot{R}_h=0$) and T^2 dependence of the reactivity, Eq. (5) reduces to

$$\frac{dp}{dt} = C_\alpha p^2, \tag{6}$$

where the right-hand side represents the alpha-particle heating and $C_\alpha > 0$. Equation (6) yields the explosive solution for $t > t_0$,

$$p(t) = \frac{p(t_0)}{1 - C_\alpha p(t_0)(t - t_0)}. \tag{7}$$

If ignition occurs, our model develops such an explosive solution even in the presence of energy losses. Equation (6) also helps to understand the difference in the heat conduction treatment in Ref. 17 as compared to our model. Reference 17 makes the same argument made in this paper (and Ref. 12) that the heat conduction losses do not cause a net energy loss (p does not depend on heat conduction) but do lead to a loss of temperature. Since in Ref. 17 ignition is defined as the condition for $dT/dt > 0$ [Eq. (26) of Ref. 17], then the heat losses do enter into the ignition condition. However, the authors of Ref. 17 also realize that ignition can occur when $dT/dt < 0$. In this case, the temperature initially decreases but eventually it reverses its course and rapidly increases. This form of ignition [which is not included in Eq. (26) of Ref. 17] can be included by defining ignition in terms of the pressure increase ($dp/dt > 0$) rather than the temperature increase ($dT/dt > 0$) as the pressure can increase even if the temperature decreases. Since our ignition model is dynamic, all the different paths to ignition are included with both pressure and temperature explosive growth.

It is useful to rewrite Eq. (5) in dimensionless form by defining the following normalization factors:

$$\tau = \frac{V_i t}{R_s}, \quad \hat{p}(\tau) = \frac{p}{p_s}, \quad \hat{R}(\tau) = \frac{R_h}{R_s},$$
$$\hat{T}(\tau) = \frac{T_0}{T_*}, \quad T_* = \left(\frac{25\mu_1}{48\pi\kappa_0} p_s R_s V_i\right)^{2/7}, \tag{8}$$

where p_s and R_s are the hot spot pressure and radius at stagnation and V_i is the implosion velocity. As shown in Sec. IV, T_* represents the stagnation temperature resulting from an adiabatic compression of the hot spot (in the absence of alpha heating and radiation losses). Here T_* has units of J with $\mu_1 \approx 0.55$ and $\kappa_0 = 3.7 \times 10^{69}\ \mathrm{m^{-1} \cdot s^{-1} \cdot J^{-5/2}}$ for $\ln \Lambda \approx 5$. For typical ICF implosion parameters, $T_*^{\mathrm{keV}} \equiv T_*/c_k$ falls in the range of 5–8 keV.

Using the power-law fit for $\langle \sigma v \rangle$ in Eq. (5) and substituting the dimensionless variables leads to the following simplified form of the energy equation:

$$\frac{d}{d\tau}(\hat{p}\hat{R}^5) = \gamma_\alpha \hat{p}^2 \hat{R}^5 \hat{T}^\sigma, \tag{9}$$

where $\gamma_\alpha = \varepsilon_\alpha C_0 / 2(1+Z)^2 c_k^{2+\sigma} p_s R_s / V_i T_*^\sigma$ is a parameter related to the initial shell condition at the beginning of the deceleration phase (Sec. III). Notice that Eq. (9) indicates that as long as the fusion reactivity $\langle \sigma v \rangle$ is proportional to $\sim T^2$ and the alpha heating rate depends only on the pressure ($n^2 \langle \sigma v \rangle \sim p^2$), then the temperature does not enter into the ignition condition. This is not the case for $\langle \sigma v \rangle \sim T^{3-4}$ since the fusion reaction rate will depend on pressure and temperature $n^2 \langle \sigma v \rangle \sim p^2 T^{1-2}$. Then, an additional equation describing the evolution of the temperature is required.

Since the pressure is determined by the pdV work and the alpha-particle heating, one can use mass conservation and the equation of state to evaluate the temperature. The evolution of the hot spot density depends on the mass ablation rate off the shell. This was first calculated in Refs. 12 and 18 and later in Ref. 19. The ablation rate can be determined by integrating the energy equation (1) across the hot spot boundary. All divergent-free terms vanish as both temperature and radiation flux approach zero at the hot spot boundary. A straightforward integration leads to

$$\frac{5}{2A} \dot{m}_a T_0 R_h^2 = \frac{6}{5} \kappa_0 T_0^{\nu+1} R_h + \mu_0 C_1 p^2 T_0^{-3/2} R_h^3, \tag{10}$$

where the ablative mass rate is $\dot{m}_a = \rho V_a = A p V_a / T$, $A = m_i/(1+Z)$, and $\mu_0 = \int_0^1 \hat{r}^2 \hat{T}^{-3/2} d\hat{r} \approx 0.85$. Notice that Eq. (10) is derived by approximating the temperature profile with a step function, the correct limit of a $\nu \gg 1$ expansion. Equation (10), accurate to order $1/\nu$, describes the energy flux balance at the hot spot boundary where the radiation and conduction energy flows are recycled back by the ablated material.

The total hot spot mass can be expressed as $M_{hs}=\int_0^{R_h}4\pi\rho r^2dr=4\pi\mu_1 ApR_h^3/T_0$, where $\mu_1\approx 0.55$ is the value of the integral $\mu_1=\int_0^1\hat{r}^2/\hat{T}d\hat{r}$, and T_0 is the hot spot central temperature. Due to mass conservation, the change of the hot spot mass is caused by the mass ablation off the shell, $dM_{hs}/dt=4\pi R_h^2\dot{m}_a$. Substituting the above results into Eq. (10) yields

$$\frac{d}{dt}\left(\frac{pR_h^3}{T_0}\right)=\frac{12\kappa_0}{25\mu_1}R_hT_0^{5/2}+\frac{2\mu_0C_1}{5\mu_1}\frac{p^2R_h^3}{T_0^{5/2}}. \tag{11}$$

Notice that this is the equation governing the hot spot temperature. The terms on the right-hand side represent the heat conduction and radiation effects on the hot spot temperature.

After a straightforward manipulation, the dimensionless form of the temperature equation can be written in the following form:

$$\frac{d}{d\tau}\left(\frac{\hat{p}\hat{R}^3}{\hat{T}}\right)=\hat{R}\hat{T}^{5/2}+\beta\frac{\hat{p}^2\hat{R}^3}{\hat{T}^{5/2}}, \tag{12}$$

where $\beta=2\mu_0C_1p_s^2T_*^{-3/2}R_s/5\mu_1p_sV_i$. Notice that β is proportional to the ratio between the total radiation energy emitted from the hot spot and the imploding shell kinetic energy. The radiation energy is proportional to $C_1p_s^2T_s^{-3/2}R_s^3\tau_c$ and the shell kinetic energy is proportional to the hot spot internal energy $MV_i^2\sim p_sR_s^3$. As shown below, the time $\tau_c\sim R_s/V_i$ represents the confinement time of the hot spot surrounded by a dense shell imploded with velocity V_i. Ignited ICF capsules require that the radiation energy be smaller than the compression work so that high temperatures can be reached in the hot spot. Furthermore, the bremsstrahlung losses are also smaller than the heat conduction losses and do not appreciably alter the temperature profile that is mostly determined by the heat conduction.

The third and last equation of our ignition model governs the conservation of momentum of the thin shell surrounding the hot spot. The thin-shell approximation (discussed in Ref. 12) assumes that the entire shell kinetic energy is transferred to the internal energy of the hot spot upon stagnation. Even though the thin-shell model overestimates the stagnation energy, it yields the correct ignition scaling. This is shown in Ref. 18, where a more accurate shell model, the so-called "thick-shell" model, is compared with the "thin-shell" one. In the thick-shell model, the shell is treated as a finite-thickness, compressible gas including the presence of a return shock driven by the rapid increase of the hot spot pressure. A similar model was also later adopted in Ref. 19. While the thick-shell model is more realistic (but more complicated) than the thin-shell one, the ignition scaling is virtually the same. Furthermore, we will use the results of Refs. 13 and 20 to heuristically limit the transfer of kinetic energy from the shell to the hot spot, which, in the thin-shell model, is overestimated (100% transfer). Within the frame of the thin-shell model, the shell compresses the hot spot like a spherical piston and the equation of motion for the shell is simply the shell Newton's law $M_s\ddot{R}=4\pi pR^2$. In dimensionless form, this equation can be rewritten using Eq. (8) as

$$\frac{d^2\hat{R}}{d\tau^2}=\hat{p}\hat{R}^2. \tag{13}$$

The shell Newton's law shows that the shell confinement time at stagnation scales as $\tau_c\sim\sqrt{M_s/p_sR_s}$. Since $M_sV_i^2\sim p_sR_s^3$, the confinement time can be rewritten as $\tau_c\sim R_s/V_i$. During this time, the hot spot hydrodynamic pressure is at its peak value (in the absence of alpha heating). The shell confinement time should not be confused with the burn time that depends on the shell areal density (Ref. 1).

Equations (9), (12), and (13) represent a dynamic model of thermonuclear ignition. The next step is to determine the relevant initial conditions for this system of equations.

III. INITIAL CONDITIONS

Based on the definition of the dimensionless variables, the initial condition of the thin-shell model requires that $\hat{R}(0)=R(0)/R_s$, $\dot{\hat{R}}(0)=-1$, $\hat{p}(0)=p(0)/p_s$, and $\hat{T}(0)=T_0(0)/T_*$, where $R(0)$, $p(0)$, $T_0(0)$ are the values of the radius, pressure, and central temperature at the beginning of the deceleration phase ($\tau=0$) when the shell is imploding inward with its maximum velocity ($dR/dt(0)=-V_i$). The stagnation values R_s and p_s can be defined through the energy conservation and adiabatic compression in the absence of alpha heating and radiation losses. In this case, energy conservation requires that $(1/2)M_sV_i^2=(4\pi/3)p_sR_s^3$, while adiabatic compression requires $p_sV_s^{5/3}=p(0)V(0)^{5/3}$ or $p_sR_s^5=p(0)R(0)^5$. Using these relations, the initial conditions for the dimensionless variables can be rewritten as $\hat{R}(0)=\varepsilon_0^{-1/2}$, $\dot{\hat{R}}(0)=-1$, and $\hat{p}(0)=\varepsilon_0^{-5/2}$, where $\varepsilon_0\equiv(1/2)M_sV_i^2/(4\pi/3)p(0)R(0)^3$ is the ratio between the shell kinetic energy and the hot spot internal energy at the beginning of the deceleration phase. Notice that $\varepsilon_0\gg 1$ in typical ICF implosions where the hot spot energy is amplified many times during the deceleration of the shell.

The initial condition for the temperature requires a special treatment. We start by integrating Eq. (12) from the beginning of the deceleration phase ($\tau=0$) to stagnation (τ_s). The stagnation values for the dimensionless variables are $\tau_s=\varepsilon_0^{1/2}$, $\hat{R}(\tau_s)=1$, $\hat{p}(\tau_s)=1$, $\hat{T}(\tau_s)=1$. The initial temperature $\hat{T}(0)$ can be inferred from an analysis of the temperature equation (12). At the beginning of the deceleration phase, both pressure and temperature are small and the radiation losses can be neglected with respect to the heat losses. Neglecting the alpha-particle heating during the hot spot assembly phase (that is, $\gamma_\alpha=0$) results in the adiabatic compression of the hot spot leading to $\hat{p}\hat{R}^5=1$. Thus, the temperature equation (12) can be rewritten as

$$\frac{d\hat{\phi}}{d\tau}=\hat{\phi}^{-5/2}\hat{R}^{-4}, \tag{14}$$

where $\hat{\phi}\equiv\hat{p}\hat{R}^3/\hat{T}$. The solution of Eq. (14) is $\hat{\phi}(\tau)^{7/2}=\hat{\phi}(0)^{7/2}+\frac{7}{2}\int_0^\tau\hat{R}^{-4}d\tau$. For large $\varepsilon_0\gg 1$, one expects the stagnation temperature to be independent of its value at the beginning of the deceleration phase (as long as the initial value is much smaller than the stagnation value). Thus, one re-

quires that $I \equiv \frac{7}{2}\int_0^{\tau} \hat{R}^{-4} d\tau \gg \hat{\phi}(0)^{7/2}$. Defining $\hat{R} = d\hat{R}/d\tau$, the integral I can be rewritten as $I = \frac{7}{2}\int_0^{\infty} \hat{R}^{-4}\dot{\hat{R}}^{-1} d\hat{R}$. Notice that most of the contribution to the integral I comes from the stagnation values $\hat{R} \approx \hat{R}(\tau_s) = 1$ and $\dot{\hat{R}} \approx \dot{\hat{R}}(\tau_s) \approx 0$. By using the shell Newton's law [Eq. (13)], one finds that $\ddot{\hat{R}}(\tau_s) \approx 1$ and the shell velocity $\dot{\hat{R}}$ can be approximated by $\dot{\hat{R}} \approx \sqrt{2(\hat{R}-1)}$ near stagnation. Substituting into I and integrating over $\hat{R}$ yields $I = 5\pi/16\sqrt{2}$. At the beginning of the deceleration phase, the initial value of $\hat{\phi}$ is $\hat{\phi}(0) = \hat{p}(0)\hat{R}(0)^3/\hat{T}(0) = (\varepsilon_0 \hat{T}(0))^{-1}$. In order to guarantee a stagnation temperature independent of its initial value, one needs to choose $\varepsilon_0^{-1} \ll \hat{T}(0) \ll 1$. Any value of $\hat{T}(0) = \varepsilon_0^{\omega}$ with $-1 < \omega < 0$ satisfies this condition, and the resulting solution of the ignition model is independent of ε_0 and ω as long as $\varepsilon_0 \to \infty$. Here we choose $\omega = 1/2$ and $\hat{T}(0) = \varepsilon_0^{-1/2} \ll 1$.

IV. SOLUTION OF THE IGNITION MODEL AND MARGINAL IGNITION CONDITION

Our ignition model consists of the three equations (9), (12), and (13) representing mass, momentum, and energy conservation, with the initial conditions derived in Sec. III. For convenience, the equations and initial conditions are summarized below,

$$\frac{d}{d\tau}(\hat{p}\hat{R}^5) = \gamma_\alpha \hat{p}^2 \hat{R}^5 \hat{T}^\sigma,$$

$$\frac{d}{d\tau}\left(\frac{\hat{p}\hat{R}^3}{\hat{T}}\right) = \hat{R}\hat{T}^{5/2} + \beta\frac{\hat{p}^2\hat{R}^3}{\hat{T}^{5/2}}, \tag{15}$$

$$\frac{d^2\hat{R}}{d\tau^2} = \hat{p}\hat{R}^2,$$

$$\hat{p}(0) = \varepsilon_0^{-5/2}, \quad \hat{T}(0) = \varepsilon_0^{-1/2}, \quad \hat{R}(0) = \varepsilon_0^{1/2}, \quad \dot{\hat{R}}(0) = -1.$$

Equations (15) are numerically solved up to the stagnation time $\tau \sim \tau_s = \varepsilon_0^{1/2}$ for a large value of $\varepsilon_0 \gg 1$, and $\sigma = 1$ is used in the computation. The solution develops an explosive instability when the parameter γ_α exceeds a critical value for a preset value of β. Here, we are interested in the asymptotic value of γ_α for $\varepsilon_0 \to \infty$ (we use $\varepsilon_0 = 10^4$ in the numerical integration). Physically, this instability corresponds to the onset of ignition. The critical values of γ_α and β are obtained through a series of numerical solutions of the system of Eqs. (15) and shown in Fig. 2, where every dot represents a single pair of γ_α and β such that the solution of the equations turns singular for both pressure and temperature. That ignition curve in Fig. 2 can be accurately fitted by the following simple formula:

$$\gamma_\alpha = 1.12 + \beta^2 + 0.28\beta^3. \tag{16}$$

Within the frame of the thin-shell model, the shell thickness is negligible. However, the effects of finite thickness can be included by noticing that only a fraction of the shell kinetic energy is converted into hot spot internal energy. That

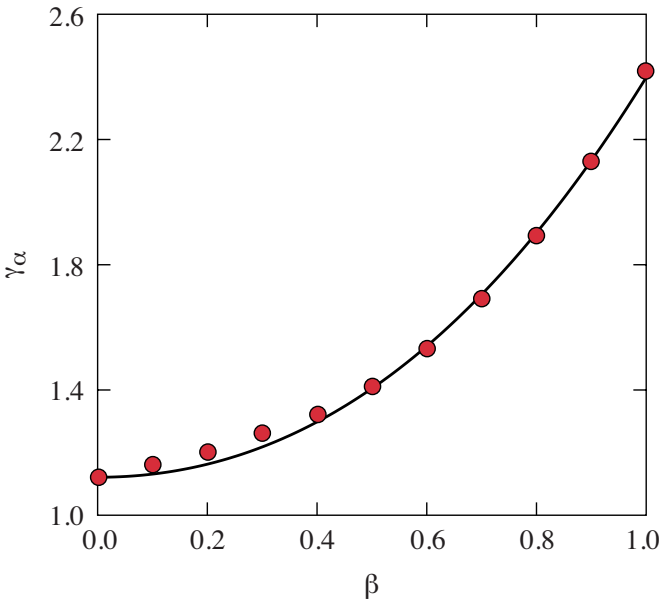

FIG. 2. (Color online) Relation between γ_α and β. Each dot represents a single pair of γ_α and β such that the solution of Eqs. (15) turns singular. The solid line is the fitting formula $\gamma_\alpha(\beta)$ in Eq. (16).

fraction is related to the ratio of the hot spot and shell volume at stagnation, and it can be written as $(1+A^{-1})^{-3}$, where A is the aspect ratio defined as the hot spot radius R_h over the shell thickness Δ, $A = R_h/\Delta$. The total mass is expressed as $M = 4\pi(\rho\Delta)R_s^2\Sigma(A)$,[20] with the volume factor Σ defined as $\Sigma(x) = 1 + (1/x) + 1/(3x^2)$. Thus, the important parameter γ_α in the ignition condition can be rewritten as

$$\gamma_\alpha = \frac{\varepsilon_\alpha C_0 T_*^\sigma}{2(1+Z)^2 c_k^{2+\sigma}} \frac{\sqrt{M}\sqrt{MV_i^2/(1+A^{-1})^3}}{4\pi R_s^2}$$

$$= \frac{\varepsilon_\alpha C_0 T_*^\sigma}{2(1+Z)^2 c_k^{2+\sigma}} \frac{\Sigma(A)}{(1+A^{-1})^{3/2}}(\rho\Delta)V_i. \tag{17}$$

Similarly, the temperature normalization factor T_* can be written as

$$T_* = \left(\frac{25\mu_1}{48\pi\kappa_0} \cdot \frac{M_s V_i^3}{R_s^2}\right)^{2/7} = \left(\frac{25\mu_1}{12\kappa_0} \cdot \frac{\Sigma(A)(\rho\Delta)V_i^3}{(1+A^{-1})^{9/2}}\right)^{2/7}. \tag{18}$$

For typical ICF implosions, the stagnation aspect ratio A usually falls within the range of $1 < A < 4$.[20] Within this interval, the function $\Sigma(A)/(1+A^{-1})^{9/2}$ can be approximated by the power law, $\Sigma(A)/(1+A^{-1})^{9/2} \approx 0.12A^{1.045}$. Since the stagnation aspect ratio scales with the implosion velocity and shell adiabat as $A \approx 8.2 \times 10^{-6} V_i^{0.96}/\alpha^{0.19}$,[13] the function $\Sigma(A)$ can be approximated as $\Sigma(A)/(1+A^{-1})^{9/2} \approx \delta_0 V_i/\alpha^{0.2}$, with the constant $\delta_0 = 5.7 \times 10^{-7}$ s/m. Substituting into Eq. (18), and solving for the implosion velocity, yields

$$V_i = \left(\frac{12\kappa_0}{25\mu_1\delta_0}\right)^{1/4} \alpha^{0.05}(\rho\Delta)^{-1/4} T_*^{7/8}. \tag{19}$$

Notice that the adiabat dependence is very weak, and it is neglected in the following derivation. Furthermore, the as-

pect ratio dependence in Eq. (17) can be approximated with a constant, $\Sigma(A)/(1+A^{-1})^{3/2}\approx 0.85$ for $1<A<4$. Substituting this result and Eq. (19) into Eq. (17), one finds the γ_α dependence on the areal density $\rho\Delta$ and temperature T_*,

$$\gamma_\alpha = \frac{0.85\varepsilon_\alpha C_0}{2(1+Z)^2 c_k^{2+\sigma}}\left(\frac{12\kappa_0}{25\mu_1\delta_0}\right)^{1/4}(\rho\Delta)^{3/4}T_*^{\sigma+7/8}. \tag{20}$$

The parameter β can be expanded in the same manner as above. Notice that $\beta/\gamma_\alpha \sim T_*^{-\sigma-3/2}$ and β can be written in the following form:

$$\beta = \frac{0.34\mu_0 C_1}{\mu_1}\left(\frac{12\kappa_0}{25\mu_1\delta_0}\right)^{1/4}(\rho\Delta)^{3/4}T_*^{-5/8}. \tag{21}$$

In both Eqs. (20) and (21), the units of $\rho\Delta$ and T_* are in $\mathrm{kg/m^2}$ and J, respectively. To express T_* in keV in these equations, γ_α and β can be rewritten as

$$\begin{aligned}
&\gamma_\alpha = C_3(\rho\Delta)^{3/4}(T_*^{\mathrm{keV}})^{15/8},\\
&C_3 = \frac{0.85\varepsilon_\alpha C_0}{2(1+Z)^2 c_k^{9/8}}\left(\frac{12\kappa_0}{25\mu_1\delta_0}\right)^{1/4},\\
&\beta = C_4(\rho\Delta)^{3/4}(T_*^{\mathrm{keV}})^{-5/8},\\
&C_4 = \frac{0.34\mu_0 C_1}{\mu_1 c_k^{5/8}}\left(\frac{12\kappa_0}{25\mu_1\delta_0}\right)^{1/4},
\end{aligned} \tag{22}$$

where $Z=1$ for DT plasma, $\varepsilon_\alpha = 3500 c_k = 5.6\times 10^{-13}$ J, $C_0 = 2.6\times 10^{-26}\ \mathrm{m^3\cdot keV^{-3}\cdot s^{-1}}$, $\mu_0 = 0.85$, $\mu_1 = 0.55$, $\kappa_0 = 3.7\times 10^{69}\ \mathrm{m^{-1}\cdot s^{-1}\cdot J^{-5/2}}$, and $\delta_0 = 5.7\times 10^{-7}\ \mathrm{m^{-1}\cdot s}$. Using $C_1 = 9.7\times 10^{-30}\ \mathrm{m\cdot J^{5/2}\cdot s^{-1}\cdot N^{-2}}$ for $Z=1$ leads to $C_4 \approx 0.327\ \mathrm{keV^{5/8}\cdot m^{3/2}\cdot kg^{-3/4}}$, and the parameter $\beta \leqslant 1$ for typical values of the areal density and temperature. Using $C_0 \approx 2.6\times 10^{-26}\ \mathrm{m^3\cdot keV^{-3}\cdot s^{-1}}$ into the first of Eqs. (22) yields $C_3 \approx 7.6\times 10^{-3}\ \mathrm{keV^{-15/8}\cdot m^{3/2}\cdot kg^{-3/4}}$ for DT fuel.

The next step is to relate the parameter T^* to the maximum temperature in the absence of alpha heating ($T_{\max}^{\mathrm{no}-\alpha}$). Such a temperature is approximately equal to the temperature measured in D_2 targets or subignited DT implosions where the self-heating plays a negligible role in the hot spot energy balance. A more detailed discussion of the validity of $T_{\max}^{\mathrm{no}-\alpha}$ as a measurable parameter is included in Sec. IX. The value of $T_{\max}^{\mathrm{no}-\alpha}$ is found by setting $\gamma_\alpha = 0$ and by solving Eqs. (15) for various values of β. The maximum of the solution for $\hat{T}$ corresponds to $T_{\max}^{\mathrm{no}-\alpha}/T_*$. A series of numerical solutions lead to the following relations between the parameter β and the maximum hot spot temperature $\hat{T}_{\max}^{\mathrm{no}-\alpha}$ without alpha heating:

$$\begin{aligned}
&\hat{T}_{\max}^{\mathrm{no}-\alpha} = \frac{T_{\max}^{\mathrm{no}-\alpha}}{T_*} = \frac{0.78}{\Pi(\beta)},\\
&\Pi(\beta) = 1 + 0.42\beta^{0.9} + 1.7\times 10^{-3}\beta^{1.8},
\end{aligned} \tag{23}$$

as shown in Fig. 3. Using Eq. (23) and the definitions of γ_α and β in Eq. (22), one can easily rewrite the ignition condition as

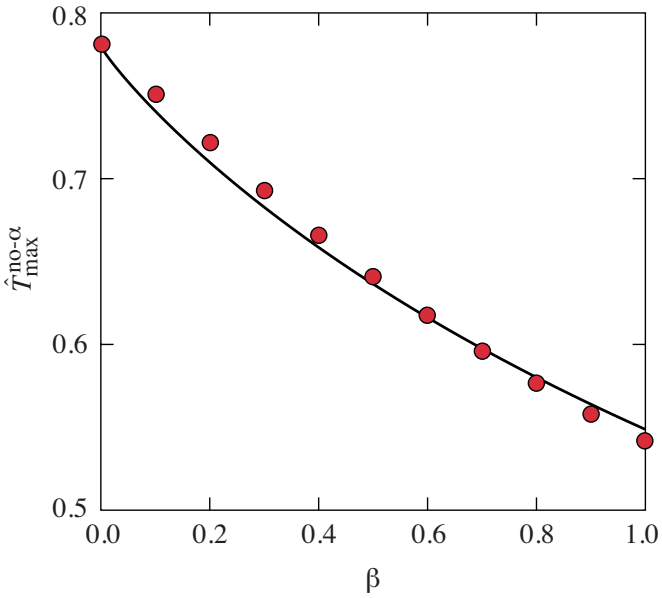

FIG. 3. (Color online) Relation between $\hat{T}_{\max}^{\mathrm{no}-\alpha}$ and β. Each dot represents a single pair of $\hat{T}_{\max}^{\mathrm{no}-\alpha}$ and β by solving Eqs. (15) with $\gamma_\alpha = 0$ for various β. $\hat{T}_{\max}^{\mathrm{no}-\alpha}$ is the maximum value of $\hat{T}$ in the solution. The solid line is the fitting formula $\hat{T}_{\max}^{\mathrm{no}-\alpha}(\beta)$ in Eq. (23).

$$(\rho\Delta)(T_{\max}^{\mathrm{no}-\alpha})^{5/2} = 33.5\frac{[\gamma_\alpha(\beta)]^{4/3}}{\Pi(\beta)^{5/2}}, \tag{24}$$

where $\rho\Delta$ is in $\mathrm{g/cm^2}$, $T_{\max}^{\mathrm{no}-\alpha}$ is in keV, γ_α is given in Eq. (16), and β can be determined in terms of $T_{\max}^{\mathrm{no}-\alpha}$ from the following equation:

$$\frac{\beta\Pi(\beta)^{5/2}}{\gamma_\alpha(\beta)} = \left[\frac{3.4}{T_{\max}^{\mathrm{no}-\alpha}}\right]^{5/2}. \tag{25}$$

Notice that for large temperatures, $T_{\max}^{\mathrm{no}-\alpha} \gg 3.4$ keV, β is small, and the ignition condition reduces to $(\rho\Delta)(T_{\max}^{\mathrm{no}-\alpha})^{5/2} = 33.5\ \mathrm{g/cm^2\,keV^{2.5}}$. By numerically solving Eq. (25) for various $T_{\max}^{\mathrm{no}-\alpha}$ in the range $2.5 < T_{\max}^{\mathrm{no}-\alpha} < 8$ keV to find β and substituting $\beta(T_{\max}^{\mathrm{no}-\alpha})$ into Eq. (24) yields the ignition condition in terms of the two measurable parameters $\rho\Delta$ and $T_{\max}^{\mathrm{no}-\alpha}$. Figure 4 shows the ignition condition in the $\rho\Delta$, $T_{\max}^{\mathrm{no}-\alpha}$ plane. A simple fit of the ignition condition, accurate to within $\pm 10\%$ in the range $4 < T_{\max}^{\mathrm{no}-\alpha} < 8$, is given by

$$(\rho\Delta) \approx \frac{2.5}{(T_{\max}^{\mathrm{no}-\alpha})^{1.18}\left[1-\left(\frac{3}{T_{\max}^{\mathrm{no}-\alpha}}\right)^{2.5}\right]}. \tag{26}$$

The solid curve in Fig. 4 shows the numerical fit in relation to the exact numerical solution of the ignition model (dots). Notice that Eq. (26) exhibits a singularity for $T_{\max}^{\mathrm{no}-\alpha} \approx 3$ keV indicating that at such low temperatures, ignition requires very large areal densities. The areal density in Eq. (26) refers to the shell areal density without including the hot spot contribution. The hot spot contribution to the areal density is typically small except for marginally ignited targets at high temperatures. As shown in Fig. 4, when $T_{\max}^{\mathrm{no}-\alpha}$ increases, the shell areal density required for marginal ignition falls below $0.5\ \mathrm{g/cm^2}$. At such low values, the shell and hot spot areal

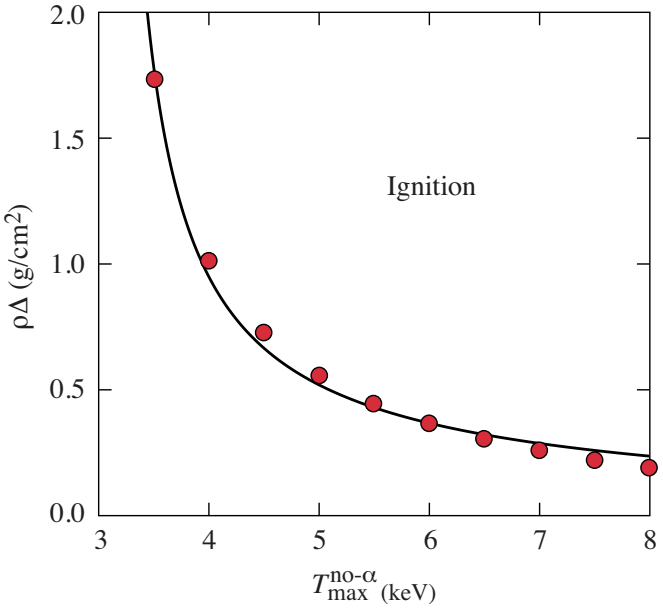

FIG. 4. (Color online) Relation between $\rho\Delta$ and $T_{max}^{no-\alpha}$ according to the ignition model of Eqs. (15). Each dot represents a single pair of $\rho\Delta$ and $T_{max}^{no-\alpha}$ from the solution of Eqs. (24) and (25) for $4 < T_{max}^{no-\alpha} < 8$. The solid line is the fitting formula in Eq. (26) and represents the marginal ignition condition.

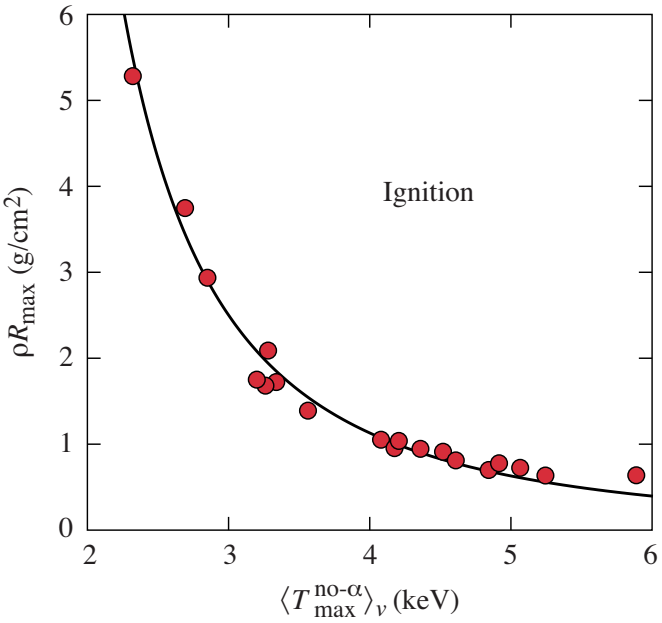

FIG. 5. (Color online) Relation between the maximum total areal density (ρR_{max}) and the maximum hot spot volume-averaged no-alpha ion temperature ($\langle T_{max}^{no-\alpha} \rangle_v$) for marginally ignited targets. Each dot represents a single simulation from the 1D hydrocode LILAC. The solid line is the fitting formula in Eq. (27).

densities are of the same order, and the hot spot contribution is a significant portion of the total areal density. In the next section, we use the total areal density from a set of hydrodynamic simulations to generate an ignition curve similar to the one in Fig. 4, and significant discrepancies between the theoretical and numerical results are expected at high ignition temperatures. A detailed discussion of the validity of Eq. (26) and a comparison with the results of numerical simulations are the subjects of the next section.

V. HYDRODYNAMIC SIMULATIONS

About 20 marginally ignited direct-drive targets have been simulated with the one-dimensional Lagrangian radiation-hydrodynamic code LILAC.[22] LILAC is routinely used for ICF target design studies at the Laboratory for Laser Energetics. It includes SESAME[23] equation of state tables, flux-limited Spitzer thermal conduction (the value of the flux limiter is set at $f=0.06$), multigroup radiation transport, multigroup alpha-particle transport, and 3D laser ray-tracing. The targets used in the simulations are spherical shells consisting of a single DT ice layer or two layers of wetted-foam $[(DT)_6CH]$ and pure DT ice. All targets are filled with 1 atm DT gas at 2.1×10^{-4} g/cm^3, and the initial aspect ratio of the targets varies from 2.0 to 5.5. The relaxation (RX) adiabat shaping[24] technique is used to design most of the laser pulse shapes for these implosions. The relaxation (RX) laser pulse consists of a prepulse followed by an interval of laser shutoff and the main pulse. Such a laser pulse is used to shape the adiabat in the ablator. In these simulations, the UV driver energy varies from 35 kJ to 10 MJ, adiabat from 0.7 to 4, implosion velocity from 1.75 to 5.3×10^7 cm/s. These targets are designed to achieve marginal ignition with the minimum laser energy. In the simulations, marginal ignition is defined as Gain=1 (fusion energy=laser energy on target). These implosions are also simulated without alpha-energy deposition to compute the areal density and the no-alpha ion temperature used in the ignition condition (Sec. IV).

Each dot in Figs. 5 and 6 shows the areal density and ion temperature of each marginally ignited target. Figure 5 shows the maximum total areal density and the maximum

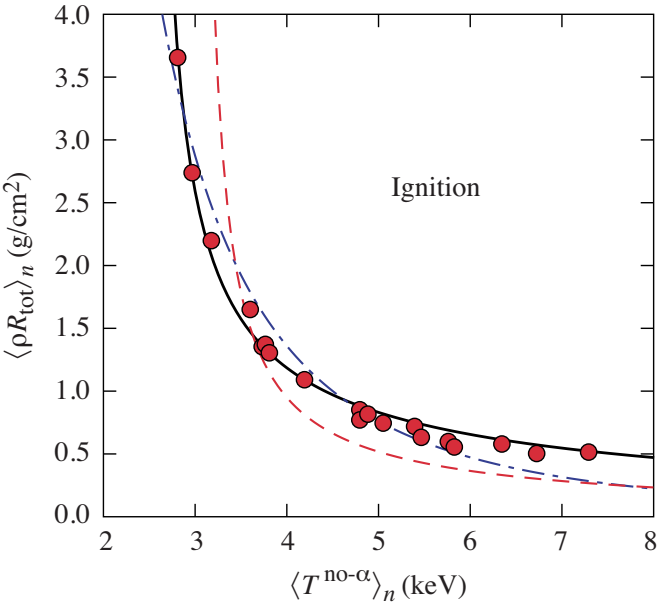

FIG. 6. (Color online) Relation between the neutron-averaged total areal density ($\langle \rho R_{tot} \rangle_n$) and the neutron-averaged no-alpha temperature ($\langle T^{no-\alpha} \rangle_n$) for marginally ignited targets. Each dot represents a single simulation from 1D hydrocode. The solid line is the fitting formula given in Eq. (28). The dashed-dotted line is the approximation of the ignition curve given in Eq. (29). The dashed curve is the ignition model given in Eq. (26) of Sec. IV.

hot spot volume-averaged no-alpha ion temperature. The hot spot is defined as the region between the center ($r=0$) and the first minimum of the temperature (or density) gradient scale length. Observe that all the points lie on a curve (i.e., the ignition curve). The latter can be accurately approximated (Fig. 5) by the following fitting formula:

$$\rho R_{\max} \approx \frac{33.5}{\langle T^{\text{no}-\alpha}\rangle_v^{5/2}\left[1-\left(\frac{1.2}{\langle T^{\text{no}-\alpha}\rangle_v}\right)^{5/2}\right]^{4/3}}, \tag{27}$$

where $\rho R_{\max}$ is in g/cm^2 and $T^{\text{no}-\alpha}$ in keV. Similarly, Fig. 6 shows the ignition points in terms of the burn-averaged areal density and the burn-averaged ion temperature. The burn-averaged areal density is defined as the total areal density weighted in time with the neutron rate. The burn-averaged temperature is the temperature weighted in time and space with the fusion reaction rate. Even in the $\langle \rho R_{\text{tot}}\rangle_n$, $\langle T_i^{\text{no}-\alpha}\rangle_n$ plane, the simulated marginal ignition points lie on an ignition curve. This curve is of particular importance since $\langle \rho R_{\text{tot}}\rangle_n$, $\langle T_i^{\text{no}-\alpha}\rangle_n$ are the only two parameters of the ICF fuel assembly that can be measured with existing techniques. The burn-averaged total areal density can be inferred from the downshift of the spectrum of charged fusion products,[10] and the burn-averaged ion temperature can be measured with the Neutron Time-of-Flight Diagnostics (nTOF).[7] One can argue that the measurements give $\langle T_i\rangle_n$ instead of $\langle T_i^{\text{no}-\alpha}\rangle_n$. However, the two parameters are virtually identical for D_2 surrogate implosions or subignited DT implosions with Gain$\ll 1$. The ignition curve in Fig. 6 can also be approximated with a simple fitting formula,

$$\langle \rho R_{\text{tot}}\rangle_n \approx \frac{3.4}{\langle T^{\text{no}-\alpha}\rangle_n^{0.97}\left[1-\left(\frac{2.5}{\langle T^{\text{no}-\alpha}\rangle_n}\right)^{2.5}\right]^{0.79}}, \tag{28}$$

where $\langle \rho R_{\text{tot}}\rangle_n$ is in g/cm^2 and $\langle T^{\text{no}-\alpha}\rangle_n$ in keV. Equation (28), which is plotted as the solid curve in Fig. 6, is the most useful form of the ignition condition that can be directly measured. A rough approximation of the ignition curve, for temperatures between 3 and 6 keV, can be cast into a simple power law,

$$\langle \rho R_{\text{tot}}\rangle_n \cdot \langle T_i^{\text{no}-\alpha}\rangle_n^{2.6} > 50\ \text{g}\cdot\text{cm}^{-2}\cdot\text{keV}^{2.6}. \tag{29}$$

The dashed-dotted line in Fig. 6 shows the simple fit (29) in relation to the simulation results (dots). To compare the ignition condition from the analytic model in Sec. IV with the simulation results, we plot Eq. (26) in the $\langle \rho R_{\text{tot}}\rangle_n$, $\langle T_i^{\text{no}-\alpha}\rangle_n$ plane of Fig. 6. The dashed curve in Fig. 6 shows the ignition model results as given in Eq. (26). This suggests that in spite of its simplicity, the ignition model captures the essential physics and the ignition condition (26) is in a reasonable agreement with the simulation results. Notice that, as expected, the model prediction (dashed curve) falls below the simulation results at high temperatures, since the hot spot areal density is not accounted for.

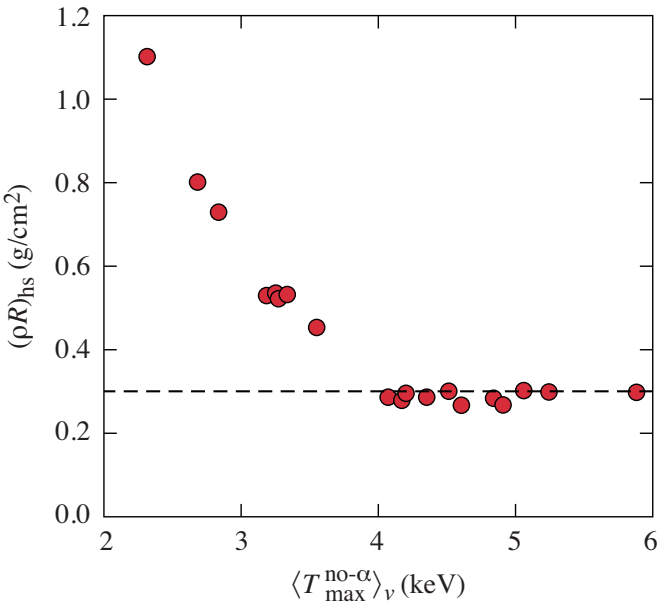

FIG. 7. (Color online) Hot spot areal density $[(\rho R)_{hs}]$ and maximum volume-averaged hot spot no-alpha ion temperature ($\langle T^{\text{no}-\alpha}\rangle_v$). Each dot represents a single simulation from 1D hydrocode. The dashed line marks the hot spot areal density of 0.3 g/cm^2.

VI. ALPHA-PARTICLE CONFINEMENT

An important assumption used in the analytic model of Sec. IV concerns the alpha-particle confinement. The assumption was made that most of the alpha particles slow down within the hot spot, and that the alpha-particle energy deposited inside the hot spot is close to 100% ($\theta\approx 1$). Since the alpha-energy deposition in the hot spot depends on its areal density and temperature,[21] we have computed the hot spot areal densities and hot spot temperature for the marginally ignited targets in our simulation database. Figure 7 shows the hot spot areal density and temperature at marginal ignition from the 1D simulations discussed in Sec. V. Observe that all the marginally ignited targets have hot spot areal density above the critical value of 0.3 g/cm^2 often cited in the literature.[1,2] To estimate the fraction of absorbed alpha particles (θ), we use the results of Ref. 21 to find that

$$\theta = \frac{3\tau}{2} - \frac{4}{5}\tau^2, \tau \leqslant \frac{1}{2};$$
$$\theta = 1 - \frac{1}{4\tau} + \frac{1}{160\tau^2}, \tau \geqslant \frac{1}{2}; \quad \tau \approx 92(\rho R)_{hs}/T_h^{3/2}, \tag{30}$$

where $(\rho R)_{\text{hs}}$ is the hot spot areal density in g/cm^2 and T_h is the hot spot temperature in keV. Substituting the areal densities and temperatures from Fig. 7 into Eq. (30) yields that the fraction of alpha energy deposited within the hot spot ranges from about 87% to 99% ($0.87<\theta<0.99$). Thus, our assumption $\theta\approx 1$ seems to be satisfied at marginal ignition. It is also interesting to observe that, as shown in Fig. 7, ignition at no-alpha temperatures ($T_h^{\text{no}-\alpha}$) below 4 keV requires a hot spot areal density well above the 0.3 g/cm^2 critical value.

For large hot spot areal densities and low hot spot temperatures, a significant fraction of the bremsstrahlung radia-

tion and conductive heat flux is absorbed within the hot spot, thus preventing a severe temperature degradation. For these targets, the only confinement issue is with the hydrodynamic disassembly of the surrounding shells. Since high hot spot areal densities are correlated with high shell areal densities,[13] the inertial confinement of such shells is very long and ignition occurs at very low no-alpha temperatures as shown in Fig. 7.

VII. COMPARISON WITH THE HTL IGNITION CONDITION

In order to test the validity of the ignition condition derived in this paper, we compare it to the ignition criterion derived by Herrmann *et al.* in Ref. 25. We refer to the criterion of Ref. 25 as the Herrmann–Tabak–Lindl (HTL) ignition condition. The HTL condition is a more accurate extension of the ignition scaling of Levedahl and Lindl[26] and it correlates the minimum shell kinetic energy required for ignition with the implosion velocity, shell adiabat, and ablation pressure. Since all our simulations are for direct-drive targets with maximum intensity around 10^{15} W/cm^2, we will use the form of the HTL condition rewritten in terms of the laser energy on target rather than the shell kinetic energy as shown in Eq. (53) of Ref. 13. The relation between laser energy and kinetic energy is $E_L=E_K/\eta$, where η is the overall hydrodynamic efficiency. For intensities of 10^{15} W/cm^2, our 1D hydrodynamic simulations show an ablation pressure close to 200 Mbar at the end of the acceleration phase in spherical implosions. Using $I_{15}=1$ and $P_L=200$ Mbar into Eq. (53) of Ref. 13, we find the following modified HTL ignition criterion:

$$E_L \approx 5.9\times 10^2 \alpha_{if}^{1.9}\left(\frac{3\times 10^7}{V_i}\right)^{6.6}, \tag{31}$$

where the laser energy E_L is in kJ and the implosion velocity V_i in cm/s. Since our ignition criterion uses the areal density and the ion temperature, a relation between these variables and those in Eq. (31) is required. For simplicity, we will consider the simplest (and the least accurate) form of our criterion, $\langle T^{\text{no}-\alpha}\rangle_n^{2.6}\cdot\langle \rho R\rangle_n > 50$ keV$^{2.6}$ g/cm^2. The scaling relations derived in Ref. 13 provide accurate formulas relating the maximum areal density and the maximum volume-averaged no-alpha temperature to the laser energy, shell adiabat, and implosion velocity. We will use the same scaling relation in Ref. 13 and simply adjust the proportionality constant to fit the neutron averaged quantities in our ignition criterion. A simple fit of the numerical results from our implosion database leads to

$$\begin{aligned}\langle \rho R\rangle_n(E_L) &= \frac{0.78}{\alpha_{if}^{0.54}}\left(\frac{V_i}{3\times 10^7}\right)^{0.06}\left(\frac{E_L}{100}\right)^{0.33},\\ \langle T^{\text{no}-\alpha}\rangle_n(E_L) &= \frac{3.5}{\alpha_{if}^{0.15}}\left(\frac{V_i}{3\times 10^7}\right)^{1.25}\left(\frac{E_L}{100}\right)^{0.07}.\end{aligned} \tag{32}$$

Figures 8 and 9 compare the results of the simulations with the above fitting formulas. Substituting Eqs. (32) into our ignition criterion yields the minimum energy required for ignition, given as

$$E_L(kJ) > 5.9\times 10^2 \alpha_{if}^{1.8}\left(\frac{3\times 10^7}{V_i}\right)^{6.5}. \tag{33}$$

Notice that the power indices and the proportionality constants in Eq. (33) are virtually identical to those in Eq. (31). This shows that our ignition criterion reproduces the HTL scaling quite accurately.

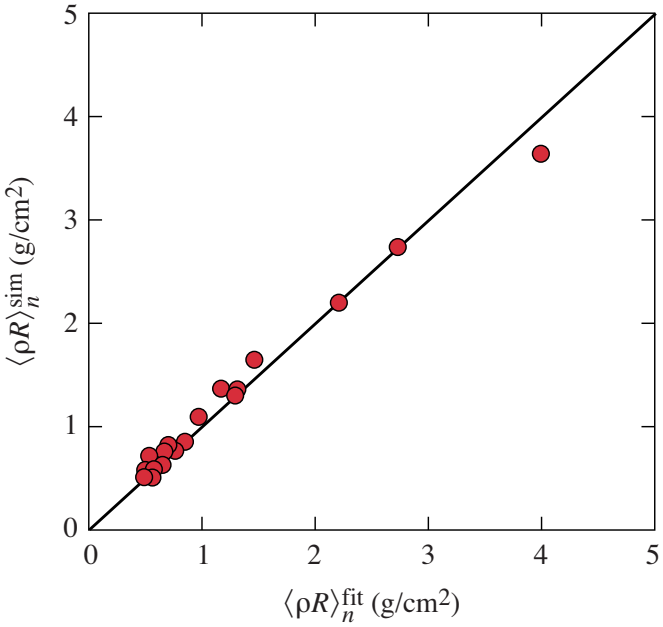

FIG. 8. (Color online) Neutron-averaged areal density $\langle \rho R\rangle_n$ from simulation (dots) compared to the numerical fit in Eq. (32) (solid line).

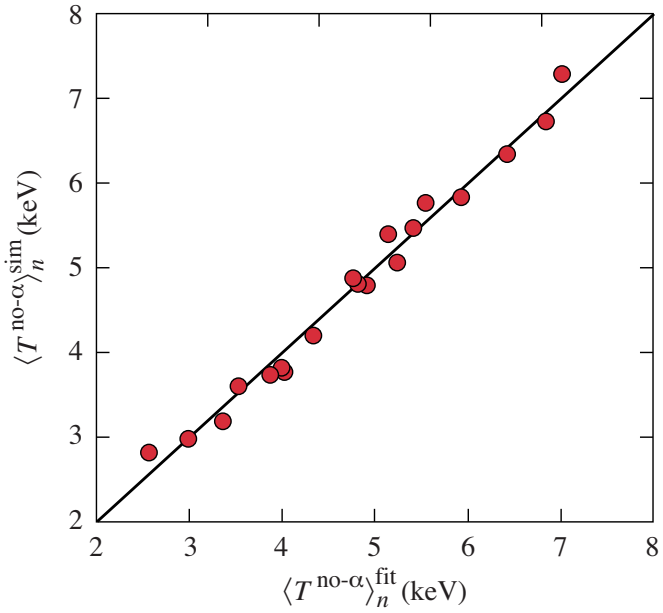

FIG. 9. (Color online) Neutron-averaged no-alpha ion temperature $\langle T^{\text{no}-\alpha}\rangle_n$ from simulation (dots) compared to the numerical fit in Eq. (32) (solid line).

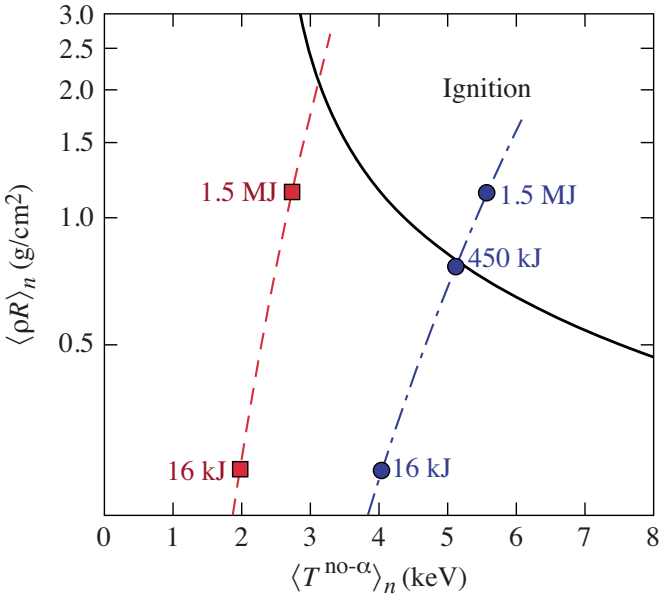

FIG. 10. (Color online) Hydro-equivalent curves in the $(\langle \rho R \rangle_n, \langle T^{\text{no-}\alpha} \rangle_n)$ plane. The solid curve is the ignition condition from Eq. (28). The dashed curve is the hydro-equivalent curve for implosions with $\alpha_{if}=2.5$, $V_i=2.4\times10^7$ cm/s from Eq. (32). The lower and upper squares are implosions at 16 kJ and 1.5 MJ, respectively. The dashed-dotted curve is the hydro-equivalent curve for implosions with $\alpha_{if}=2.7$, $V_i=4.25\times10^7$ cm/s. Three dots are implosions at 16 kJ, 450 kJ, and 1.5 MJ.

VIII. HYDRO-EQUIVALENT CURVES

In this section, we introduce the concept of hydro-equivalency and hydro-equivalent curves in the ρR, $T^{\text{no-}\alpha}$ plane. ICF targets with similar in-flight hydrodynamic variables, but different driver energy and gain, are considered hydrodynamically equivalent. Hydro-equivalent targets are expected to exhibit the same hydrodynamic behavior with respect to their hydrodynamic performance not only in 1D but also in 3D. Here, we relate the hydrodynamic performance to the peak pressure of the stagnating core and to the hydrodynamic stability of the implosion. If a set of targets is scaled in mass (M), radius (R), thickness (Δ), adiabat (α), implosion velocity (V_i), laser intensity (I), and energy (E_L) according to the simple scaling $M\sim E_L$, $R\sim E_L^{1/3}$, $\Delta\sim E_L^{1/3}$, $I\sim$ const, $\alpha\sim$ const, and $V_i\sim$ constant, then the target implosions yield the same peak pressure and the same hydrodynamic stability properties. The latter is related to the magnitude of the in-flight-aspect-ratio (IFAR) that depends on the implosion velocity, adiabat, and laser intensity (Ref. 13). Assuming the same relative size of the initial perturbations on targets, hydro-equivalent targets have the same Rayleigh–Taylor growth factor (Ref. 13) and the same RT amplitude with respect to their thicknesses. As shown in Eqs. (32) (and in Ref. 13), due to the dependence on the laser energy E_L, hydro-equivalent targets will produce different areal densities and slightly different no-alpha temperatures. Obviously, targets imploded by larger drivers (larger E_L) will achieve greater ρR and $T^{\text{no-}\alpha}$.

Using Eqs. (32), one can easily plot hydro-equivalent curves on the $\langle \rho R \rangle_n$, $\langle T^{\text{no-}\alpha} \rangle_n$ ignition plane, by fixing α and V_i in Eqs. (32) and letting E_L vary. In Fig. 10, we plot two hydro-equivalent curves for the direct-drive NIF point design[27] and the high areal-density cryogenic D_2 implosions on the OMEGA laser.[8] The direct-drive NIF point design has an in-flight adiabat of 2.7 and implosion velocity of 4.25×10^7 cm/s. The hydro-equivalent curve for such values of α_{if} and V_i is the dashed-dotted curve in Fig. 10. The bottom dot on such a curve is the hydro-equivalent point for a 16 kJ implosion. The areal density and no-alpha temperature corresponding to that point are $\langle \rho R \rangle_n \approx 0.25$ g/cm^2 and $\langle T^{\text{no-}\alpha} \rangle_n \approx 4.1$ keV. The top dot on the same curve represents the same implosion scaled up to NIF-like energies of 1.5 MJ. The middle dot is the same implosion scaled up to 450 kJ. Notice that the 450 kJ implosion is right on the 1D marginal ignition curve that is the solid curve in Fig. 10. This shows that the full NIF energy of 1.5 MJ is approximately three times higher than required for 1D marginal ignition. The main implication of the plots in Fig. 10 is the following. If a 16 kJ cryogenic implosion is carried out on the OMEGA laser to achieve areal densities and temperatures as indicated on the bottom point, then one can use such a result to theoretically conclude that the same implosion scaled up to the NIF will have three times more energy as required by the 1D Lawson criterion. While this is not an absolute proof that such a target will ignite on the NIF, it will establish some confidence in the achievement of ignition.

The point representing the high areal-density cryogenic implosions on the OMEGA laser[8] is the bottom square on the dashed curve. That point represents a neutron averaged areal density slightly exceeding 0.2 g/cm^2 and neutron averaged temperature of 2 keV. The corresponding implosion had an in-flight adiabat of about 2.5 and implosion velocity of about 2.4×10^7 cm/s. The upper square on that hydro-equivalent curve is below the marginal ignition curve and it represents the same implosion scaled up to the full NIF energy of 1.5 MJ. Such an implosion would fail to ignite. This is explained by the relatively low implosion velocity ($V_i\approx2.4\times10^7$ cm/s) and by the sensitivity on V_i of the minimum energy required for ignition [see Eq. (33)]. Current OMEGA cryogenic targets[8] are massive shells (430 μm outer diameter) with a 95-μm-thick cryogenic layer and a 10-μm-thick plastic ablator used to study high compression while reducing the effect of hydrodynamic instabilities.

In summary, hydro-equivalent curves plotted on the ρR, $T^{\text{no-}\alpha}$ ignition plane are useful to predict 1D performance for different laser energies. An immediate conclusion is that OMEGA-size capsules will have to be imploded at higher implosion velocities (for the same adiabat) to achieve a hydro-equivalent demonstration of ignition.

IX. CONCLUSIONS

Equation (28) provides an accurate representation of a measurable Lawson criterion for inertial confinement fusion with DT fuel. Such an ignition condition is found using an analytic dynamic model of ignition, and it is confirmed by the results of one-dimensional simulations of marginally ignited direct-drive targets (Gain$\approx$1). A simple fit of the ignition condition can be written as

$$\langle T^{\text{no}-\alpha}\rangle_n^{2.6} \cdot \langle \rho R_{\text{tot}}\rangle_n > 50\ \text{keV}^{2.6} \cdot \text{g/cm}^2. \quad (34)$$

This ignition condition is given in terms of the only two measurable parameters of the compressed fuel: (i) the burn-averaged total areal density $\langle \rho R_{\text{tot}}\rangle_n$, and (ii) the neutron-averaged hot spot ion temperature $\langle T^{\text{no}-\alpha}\rangle_n$ without accounting for the alpha-particle energy deposition. The burn-averaged total areal density can be measured through the detection of the spectrum of fusion products such as protons from secondary reactions.[10] The neutron-averaged temperature is measured through the Neutron Time-of-Flight diagnostic.[7] In our ignition condition, the neutron-averaged ion temperature is computed without the contribution of the fusion alpha particles. This is done to avoid using the actual temperature that undergoes extremely large and sudden variations when the compressed fuel assembly approaches the ignition condition. The so-called no-alpha temperature $T^{\text{no}-\alpha}$ used in this paper is a slowly varying hydrodynamic parameter that is well suited to measure the implosion performance with respect to the ignition condition. The only drawback for using $T^{\text{no}-\alpha}$ rather than T is that $T^{\text{no}-\alpha}$ is not always equal to the actual measurable temperature. The no-alpha temperature and the real temperature are virtually identical for cryogenic implosions with surrogate fuel (such as D_2) and for subignited DT implosions with gains much less than unity. In both cases, the fusion self-heating is negligible and $T^{\text{no}-\alpha} \approx T$. For DT implosions approaching ignition (gains $\geqslant 0.1$), the alpha heating plays an important role in determining the hot spot temperature and our form of the Lawson criterion cannot be used. However, in this case the neutron yield measurement alone is sufficient to determine that the implosion is approaching ignition. Because of the large excursion in neutron yield of a target approaching ignition (commonly referred to as the "ignition cliff"), the neutron yield rather than a formula like Eq. (34) is a better indicator of the target performance.

The measurable Lawson criterion Eq. (34) compares favorably with the Herrmann–Tabak–Lindl ignition scaling when the areal density and temperature are rewritten in terms of the implosion velocity, in-flight adiabat, and driver energy by using the conversion formulas (32) (also from Ref. 13). Furthermore, hydro-equivalent curves [Eqs. (32)] are plotted on the ignition diagram to show how hydro-equivalent implosions would perform with respect to the ignition condition when scaled-up in laser energy.

Note that the ignition model presented here could be modified according to the results in Ref. 28 to include the effects of hydrodynamic instabilities developing at the hot spot–shell interfaces. Another option is to use the ratio of the measured neutron yield to the predicted 1D yield (the YOC or yield-over-clean) to infer the effects of hydrodynamic instabilities. Such an extension of the ignition model is in progress at the Laboratory for Laser Energetics Fusion-Science-Center and it will lead to a more accurate ignition condition that is valid in multidimensions.

ACKNOWLEDGMENTS

The authors wish to thank Professor D. Shvarts for many useful discussions.

This work has been supported by the U.S. Department of Energy under Cooperative Agreement Nos. DE-FC02-04ER54789 (Fusion Science Center supported by the Office of Fusion Energy Sciences) and DE-FC03-92SF19460 (Office of Inertial Confinement Fusion), the New York State Energy Research Development Authority, and the University of Rochester.

[1] S. Atzeni and J. Meyer-ter-Vehn, *The Physics of Inertial Fusion* (Clarendon, Oxford, 2004).
[2] J. D. Lindl, *Inertial Confinement Fusion* (Springer, New York, 1998).
[3] J. D. Lawson, Proc. Phys. Soc. London, Sect. B **70**, 6 (1957).
[4] S. Atzeni and A. Caruso, Phys. Lett. **85A**, 345 (1981).
[5] S. Yu. Gus'Kov, O. N. Krokhin, and V. B. Rozanov, Nucl. Fusion **16**, 957 (1976).
[6] R. Kishony, E. Waxman, and D. Shvarts, Phys. Plasmas **4**, 1385 (1997).
[7] V. Yu. Glebov, D. D. Meyerhofer, C. Stoeckl, and J. D. Zuegel, Rev. Sci. Instrum. **72**, 824 (2001).
[8] T. C. Sangster, V. N. Goncharov, P. B. Radha, V. A. Smalyuk, R. Betti, R. S. Craxton, J. A. Delettrez, D. H. Edgell, V. Yu. Glebov, D. R. Harding, D. Jacobs-Perkins, J. P. Knauer, F. J. Marshall, R. L. McCrory, P. W. McKenty, D. D. Meyerhofer, S. P. Regan, W. Seka, R. W. Short, S. Skupsky, J. M. Soures, C. Stoeckl, and B. Yaakobi, Phys. Rev. Lett. **100**, 185006 (2008).
[9] T. R. Boehly, D. L. Brown, R. S. Craxton, R. L. Keck, J. P. Knauer, J. H. Kelly, T. J. Kessler, S. A. Kumpman, S. J. Loucks, S. A. Letzring, F. J. Marshall, R. L. McCrory, S. F. B. Morse, W. Seka, J. M. Soures, and C. P. Verdon, Opt. Commun. **133**, 495 (1997).
[10] F. H. Seguin, C. K. Li, J. A. Frenje, D. G. Hicks, K. M. Green, S. Kurebayashi, R. D. Petrasso, J. M. Soures, D. D. Meyerhofer, V. Yu. Glebov, P. B. Radha, C. Stoeckl, S. Roberts, C. Sorce, T. C. Sangster, M. D. Cable, K. Fletcher, and S. Paladino, Phys. Plasmas **9**, 2725 (2002).
[11] M. D. Campbell and W. J. Hogan, Plasma Phys. Controlled Fusion **41**, B39 (1999).
[12] R. Betti, M. Umansky, V. Lobatchev, V. N. Goncharov, and R. L. McCrory, Phys. Plasmas **8**, 5257 (2001).
[13] C. D. Zhou and R. Betti, Phys. Plasmas **14**, 072703 (2007).
[14] D. Mihalas and B. W. Mihalas, *Foundations of Radiation Hydrodynamics* (Oxford University Press, Oxford, 1984).
[15] Ya. B. Zel'dovich and Yu. P. Raizer, *Physics of Shock Waves and High-Temperature Hydrodynamic Phenomena* (Dover, Mineola, NY, 2002).
[16] H. S. Bosch and G. M. Hale, Nucl. Fusion **32**, 611 (1992).
[17] S. Atzeni and A. Caruso, Nuovo Cimento Soc. Ital. Fis., B **80**, 71 (1984).
[18] R. Betti, K. Anderson, V. N. Goncharov, R. L. McCrory, D. D. Meyerhofer, S. Skupsky, and P. P. J. Town, Phys. Plasmas **9**, 2277 (2002).
[19] Y. Saillard, Nucl. Fusion **46**, 1017 (2006).
[20] R. Betti and C. Zhou, Phys. Plasmas **12**, 110702 (2005).
[21] O. N. Krokhin and V. B. Rozanov, Sov. J. Quantum Electron. **2**, 393 (1973).
[22] J. Delettrez, R. Epstein, M. C. Richardson, P. A. Jaanimagi, and B. L. Henke, Phys. Rev. A **36**, 3926 (1987).
[23] S. P. Lyon and J. D. Johnson, Los Alamos National Laboratory Report No. LA-UR-92–3407, Los Alamos, NM, 1992, NTIS Order No. DE85014241.
[24] K. Anderson and R. Betti, Phys. Plasmas **11**, 5 (2004).
[25] M. C. Herrmann, M. Tabak, and J. D. Lindl, Nucl. Fusion **41**, 99 (2001).
[26] W. K. Levedahl and J. D. Lindl, Nucl. Fusion **37**, 165 (1997).
[27] P. W. McKenty, V. N. Goncharov, R. P. J. Town, S. Skupsky, R. Betti, and R. L. McCrory, Phys. Plasmas **8**, 2315 (2001).
[28] J. Sanz, J. Garnier, C. Cherfils, B. Canaud, L. Masse, and M. Temporal, Phys. Plasmas **12**, 112702 (2005).